CFD Simulations of the New MEXICO Rotor Experiment under Yawed Flow

IOP Conf. Series: Journal of Physics: Conf. Series **1037** (2018) 022031 doi:10.1088/1742-6596/1037/2/022031

CFD Simulations of the New MEXICO Rotor Experiment under Yawed Flow

Manfred Imiela

Lilienthalplatz 7, 38108 Braunschweig, Germany

manfred.imiela@dlr.de

Abstract. This paper describes the conduction of CFD simulations with DLR's flow solver TAU for comparison with the experimental data that has been used within the third phase of the MexNext-III project. More precisely computations for three different inflow velocities under yawed flow condition have been conducted and compared to the experimental results. Important aspects of the simulations such as a sufficiently long simulation time or a sufficiently small time-step are discussed. At first local flow quantities such as the flow velocity along axial and radial traverses, pressure distributions at four radial stations and normal and tangential forces at these sections are compared. Subsequently the integral rotor quantities i.e. rotor thrust and rotor torque are revised. The integration of the CFD results is performed using the complete surface dataset as well as two subsets. The comparison proves that the agreement can substantially be improved if the subset resembles the experimental dataset. Furthermore the integration of the experimental dataset is reviewed and a weak spot in the current reconstruction procedure of the trailing edge pressure is identified. The proposed alternative provides evidence that further improvements are possible. The final comparison shows an acceptable agreement for the medium and high inflow speed case yielding 0% and 10% difference for integral thrust and 9% and 14% for integral torque. The results for the low inflow speed case are divers: while the agreement for the integral thrust is excellent, it is less satisfactory for the integral torque which amounts to 41%.

1. Introduction

Today CFD codes for predicting the flow around wind turbines and the forces exerted on their blades are widely used in research laboratories around the world. One essential issue for increasing the confidence in the predictive capabilities of these codes constitutes a sound code validation. This can be achieved through detailed comparisons between numerical results and experimental measurements. Amongst these experiments the NREL Phase-VI turbine is probably the most widely known due to the size of the model (D_{Rotor} = 10m). The MEXICO project described in [1] and the New MEXICO experiment presented in [2] were carried out in the Large Scale Low Speed Facility (LLF) of the German Dutch Wind Tunnels (DNW) in 2006 and 2014 respectively. Although the diameter of the MEXICO rotor measures only half the size of the NREL Phase-VI turbine, it serves well as a coherent database for aerodynamic validation because PIV measurements of axial and radial traverses were recorded besides the regular pressure sensors on the blade. While quite a number of papers have been published examining the axial flow cases, e.g. [6], [7], [8], [10] and [11], publications of the yawed flow experiments are found much more rarely, e.g. [9]. The goal of the present paper is therefore to fill this gap by providing an in-depth comparison between the experimental results and the simulations.

2. Description of the experimental setup

The experimental database comprises various test cases for dynamic inflow, non-uniformity between the blades, yawed flow effects, parked conditions, pitch misalignment and blade add-ons. Pressure measurements on the rotor blades have been acquired using 148 kulites distributed over five radial stations. Instantaneous velocities along axial and radial traverses have been recorded by PIV measurements. Within the IEA Wind Task 29 three test cases for yawed flow were chosen for comparison with numerical simulations. For these test cases the rotor was yawed 30° into the wind if the rotor blade is regarded at an azimuthal position of 270° (equivalent to 9 o'clock position if looking in downwind direction). In all cases the rotor is spinning at a rotational speed of 425.1 rpm. All blades are pitched nose-up by 2.3°. As shown in **Table 1** only the inflow velocity varies from 10 m/s for the low inflow speed over 15 m/s to 24 m/s for the high inflow velocity. The other quantities can be regarded as constant. A zigzag strip was applied on the pressure and suction side on all rotor blades from 20% to 70% radius to ensure laminar to turbulent transition. A detailed description of the blade design and further information on the experimental campaign can be found in [3].

Table 1: Experimental test conditions for the three yawed test cases

Case	Yaw (°)	V_{tunnel} (m/s)	ρ (kg/m^3)	T_{inf} (°K)	P_{inf} (N/m^2)
2.1	30	10.03	1.198	293.93	101612
2.2	30	15.01	1.198	294.16	101625
2.3	30	24.08	1.198	293.92	101595

3. CFD Solver TAU

The TAU-Code [5] developed at the Institute of Aerodynamics and Flow Technology is used for the aerodynamic simulations. It solves the compressible, three-dimensional Reynolds-Averaged Navier-Stokes (RANS) equations using a finite volume formulation. The TAU-Code uses a cell-vertex formulation with a dual-grid approach for the spatial discretization. The solver module contains a central scheme as well as several upwind schemes for the discretization of the inviscid fluxes. Viscous terms are computed with a second-order central scheme. For artificial dissipation scalar or matrix dissipation might be selected. For the simulation of turbulent flows several one- and two-equation turbulence models are implemented.

Time integration is achieved using either an explicit Runge-Kutta type time-stepping scheme or an implicit LU-SGS (lower-upper symmetric Gauss-Seidel) algorithm. Time-accurate simulations are performed with a dual-time stepping approach. Various multi-grid type cycles are available for accelerating the convergence of the flow equations.

In case of multi-block meshes arbitrary motions can be prescribed for each mesh block by the motion module. The chimera technique additionally allows for overlapping of different mesh blocks and therefore eases the mesh generation process.

4. Description of the numerical setup

The computations have been carried out in URANS mode using the implicit LU-SGS algorithm in combination with the dual-time stepping approach. Acceleration of the computations was achieved through a 3v multigrid cycle as well as significant parallelization. In order to reach second order accuracy the central scheme in combination with matrix dissipation was selected. The overset grid approach and the motion module were adopted to account for the overlapping meshes and the relative motion, i.e. the background grid was kept stationary while the three blade meshes rotate around the origin. The numerical setup was simplified in order to reduce the effort for the time consuming

simulations. Therefore neither the nacelle nor the tower nor the spinner has been considered in the computations. It will be shown later that the nacelle has a non-negligible effect which was also shown earlier in [9] by Sørensen. Unfortunately the inclusion of the nacelle was not possible due to time constraints in the project. **Figure 1** presents the complete mesh that is comprised of the background grid and three blade meshes. The cylindrical background mesh measures 16 rotor diameters in diameter and 16 rotor diameters from inflow to outflow (8 rotor diameters from inflow to rotor plane). **Figure 2** shows the meshing topology of the background grid and the applied boundary conditions. While hexahedral elements were used for the inner part of the background grid, tetrahedral elements were used to fill the remaining area between the inner part and the farfield. The structured domain extends slightly beyond the PIV measurement region, i.e. three rotor diameters upstream and downstream of the rotor plane and 3m to each side of the rotor. The blade surface of the rotor is defined as no-slip wall, while farfield conditions are applied on the complete outer mesh surface. For simplicity the most inner part of the background grid is modelled with a solid cylinder with a diameter of ten centimeters. This simplification can be regarded as critical for the yawed flow cases since the inner cylinder will influence the incoming flow as well as the wake behind the turbine. On the other hand the size of the cylinder is diminutive and therefore limiting the effect on the other part of the flow domain. The reason for this simplification was to avoid a mesh singularity at the axis of the cylindrical background grid as well as ill-conditioned cells that can occur close to the axis. A slip-wall (Euler) condition was set on the outer surface of this inner cylinder.

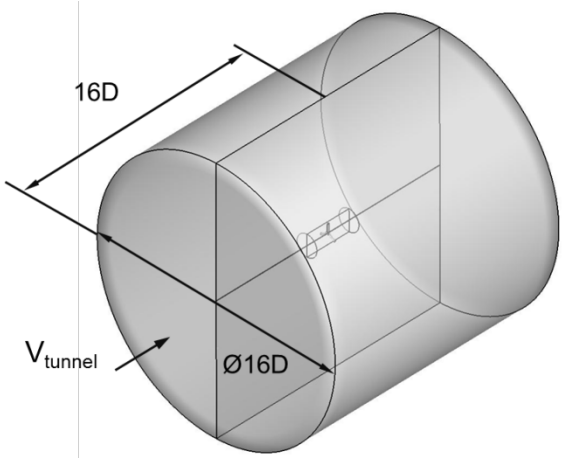

Figure 1: Global mesh setup (including blade and background meshes) and farfield distances

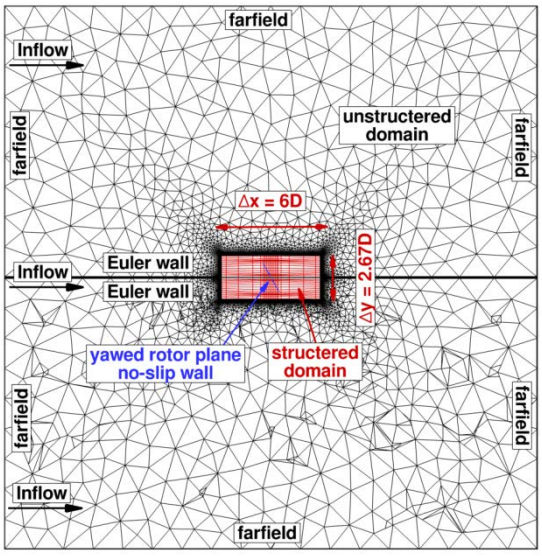

Figure 2: Meshing topology and boundary conditions

Figure 3 depicts a close-up of the structured near blade region showing the grid resolution in the vicinity of the rotor plane and describing the location of the axial and radial traverses in the experiment. As can be seen in **Figure 3** the axial traverses (green lines) for the PIV measurements are located 1.5m to each side of the non-yawed rotor axis measured in the tunnel coordinate system (tcs) and extend 4.5m up- and 5.9m downstream of the rotor center. The radial traverses are aligned parallel to the yawed rotor plane with a distance of ±0.3m to the rotor measured in the model coordinate system (mcs). In radial direction the traverses extend 3m to each side of the rotor center measured in the model coordinate system and therefore extend some 70 centimeters beyond the rotor tips. The grid resolution in the structured background domain close to the tips was set to 4mm in lateral and 10mm

in longitudinal direction and therefore compares well with the spatial measurement resolution. For the background grid a total of 23 million grid points have been used. The rotor blade mesh is generated based on the official CAD geometry from the Epos site. Hexahedral elements have almost exclusively been used for the meshing, because they are well-suited for geometries with high aspect ratios and also ease the post-processing. **Figure 4** shows the surface mesh of the rotor blade containing 145 points in radial and 272 points in chordwise direction. With 60 points in the normal direction each blade mesh is made-up of approximately 2.4 million points. Therefore the total mesh consists of 30.2 million points. Although no mesh convergence study on the number of points has been carried out, the present mesh can be regarded as mesh-independent if compared with the results in [9] by Sørensen. Moreover the mesh resolution compares very well with the mesh resolution from most other partners as can be seen in appendix F of [4]. While the University of Stuttgart used a much finer mesh, the differences in results are only small.

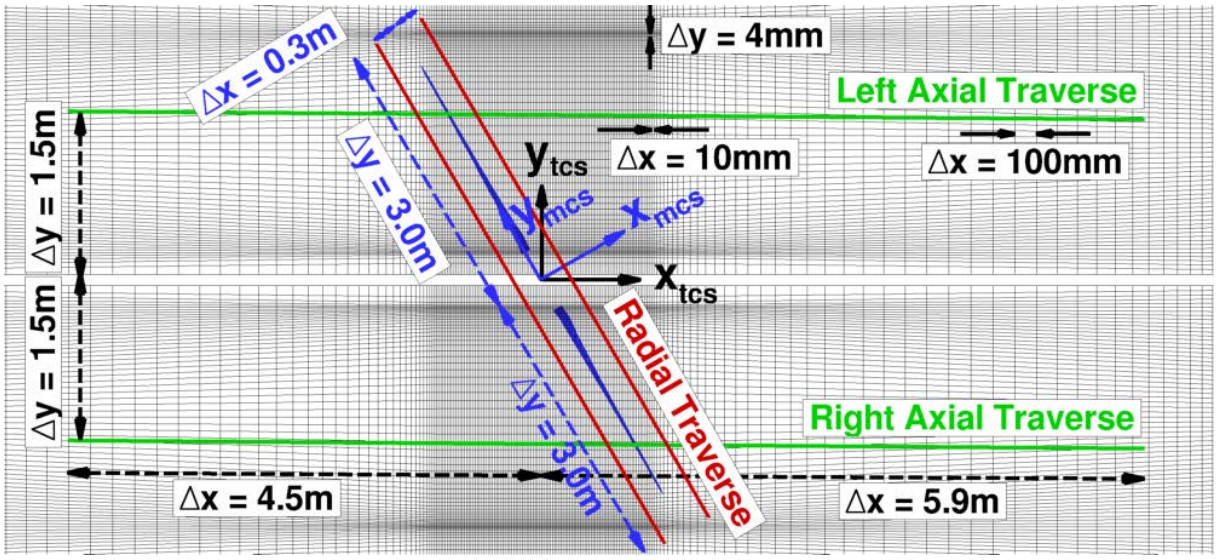

Figure 3: Structured near blade region with description of background grid resolution and location of axial and radial traverses as used for the PIV measurements in the experiment (topview)

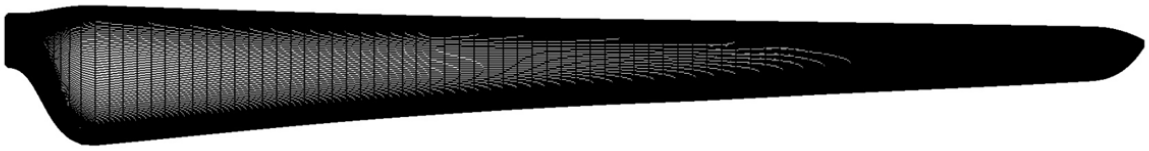

Figure 4: Blade surface mesh (radial*chordwise points = 145*272)

5. Comparison of experimental and numerical results

The numerical simulations have been carried out as much in concordance with the experiment as possible. One of the biggest simplifications is probably the negligence of the nacelle and the zigzag strip since this would have added much complexity to the simulations. Selecting a fully turbulent boundary layer computation proofs to be a conservative assumption as was previously shown by Heister [11] during the second comparison round for the axial flow cases. Concerning the turbulence model Menter's k-ω SST model yields superior results for separated flows than the Wilcox k-ω turbulence model as shown by Menter in [12]. The simulations undertaken by Heister [11] for axial flow support this fact clearly. The global time step for case 2.1 and 2.2 was chosen based on experience to be $3.92*10^{-4}$ s which is equivalent to 1° azimuth. Comparing the time step with the

choice of other partners within the MexNext consortium (see appendix F in [4]) this seems to be reasonable.

Table 2: Settings for the numerical simulations

Case	Turbulence Model	Transition Type	Turbulent Intensity [%]	P_{inf} (N/m^2)	Time Step [s]
2.1	k-ω SST	fully turbulent	0.4	101081	$3.92*10^{-4}$
2.2	k-ω SST	fully turbulent	0.4	101181	$3.92*10^{-4}$
2.3	SA_{neg} k-ω SST	fully turbulent fully turbulent	0.4 0.4	101060 101060	$3.92*10^{-4}$ $1.96*10^{-5}$

In a first approach the same time step was also used for case 2.3 in combination with the SA_{neg} turbulence model. Since the obtained results were quite disappointing, a small time step investigation (analyzing azimuthal resolutions of 1.0°, 0.5°, 0.25° and 0.05°) was conducted in order to determine the sufficient temporal discretization. The analysis disclosed that reducing the azimuthal resolution from 0.25° to 0.05° resulted in only minor changes of the torque coefficient at the end of each time step. Because the comparison was only carried out for a few azimuth positions, the smaller temporal resolution (resulting in a time step of $1.96*10^{-5}$ s) was adopted for case 2.3 as a conservative choice. The smaller time step improved the stability of the simulation because it reproduced much better the unsteady phenomena which are more prominent in case 2.3 due to the higher inflow velocity. If the improved accuracy has to be accounted to the smaller time step or the turbulence model cannot clearly be distinguished. The turbulent intensity in the wind tunnel was unfortunately only measured in the 8 x 6 m² open test section and extrapolated for the 9.5 x 9.5 m² test section. Since the turbulent intensity for the 9.5 x 9.5 m² test section was not exactly known an intermediate value of 0.4% was used for the numerical simulations. In any case the influence of the turbulent intensity at the farfield in the numerical simulation should be small because the fully turbulent mode chosen for the simulation. In comparison to the experiment the pressure at the farfield had to be slightly adjusted since the values given in **Table 1** do not fulfill the ideal gas law. The selected settings for the calculations are summarized in **Table 2**.

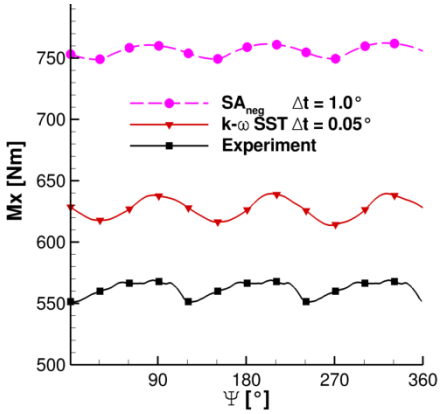

Figure 5: Rotor torque (Mx) of the last revolution for case 2.3 integrated over all surface mesh points of the CFD solution: experiment (black, squares), k-ω SST model with 0.05° resolution (red, gradients) and SA_{neg} model with 1.0° resolution (purple, circles)

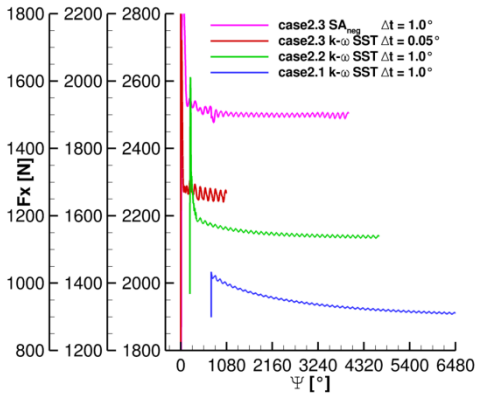

Figure 6: Convergence of the rotor thrust (Fx) as a function of the rotor azimuth angle Psi for all inflow conditions and two turbulence models. Integration over all surface mesh points of the solution (case 2.1 = left ordinate, case 2.2 = middle ordinate, case 2.3 = right ordinate)

The results of the TAU simulations for test case 2.3 in **Figure 5** reveal a clear effect of the choice of the time step and/or turbulence model. Although the torque discrepancy still amounts to 11.6% even for the simulation with the small time step and k-ω SST turbulence model, the relative error was diminished from an initial value of 34.5%. Moreover the torque amplitude that is observed over one revolution is much better captured by the simulation with the small time step. Another important issue concerns the simulation time. As can be seen in **Figure 6** the required simulation time varies amongst the different cases. While the relative error in thrust for case 2.1 (blue line, left ordinate) still amounts to 0.1% per revolution after 18 revolutions, the relative error for case 2.2 (green line, middle ordinate) falls below 0.1‰ after less than 12 revolutions and for case 2.3 (red and purple line, right ordinate) only 3 revolutions are needed to reach the same convergence limits as in case 2.1 after 18 revolutions.

5.1. Axial and radial traverses

The axial velocities extracted from the axial traverses for the three flow cases are depicted in **Figure 7** (left traverse) and **Figure 8** (right traverse). Both measurements (and the results from the simulation) are recorded **instantaneously** 30° before blade passage. This means that in the case of the left traverse the rotor is located at the 0° azimuth position. In this situation the first blade is pointing upwards as depicted in **Figure 9** by the green rotor. In the case of the right traverse the rotor is positioned at 60° azimuth angle meaning blade 1 has rotated 60° in clockwise rotation as shown by the blue rotor in **Figure 9**.

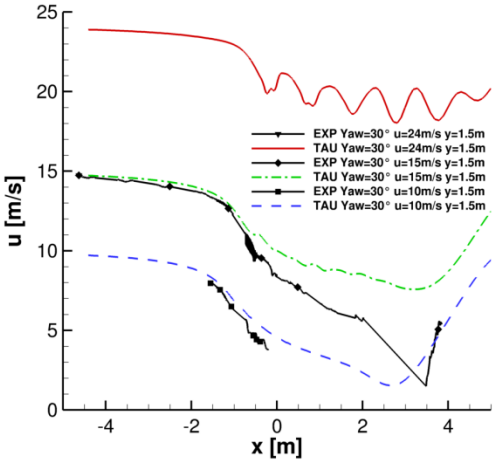

Figure 7: Streamwise velocity component (u) of the **left** axial traverse for all flow cases (case 2.3: solid red line; case 2.2: dotted dashed green line; case 2.1: dashed blue line)

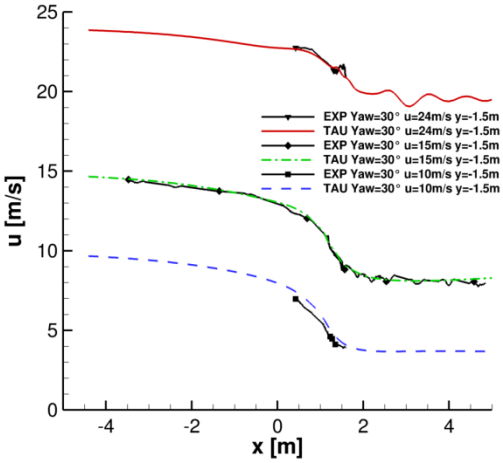

Figure 8: Streamwise velocity component (u) of the **right** axial traverse for all flow cases (case 2.3: solid red line; case 2.2: dotted dashed green line; case 2.1: dashed blue line)

As can be seen the agreement is excellent for the right traverse. The biggest velocity difference of 0.5 m/s occurs for case 2.1. The best traverse measurements were achieved for case 2.2 where the measured values range from x = -4 to +5 m. The agreement between TAU and the experiment is excellent for the complete traverse. Less accordance is found for the left traverse. While the measurements and the simulation still compare fairly well for case 2.1, the differences increase severely for case 2.2. Clearly the simulation overestimates the velocities behind the turbine. The reason for this is the negligence of the spinner and the nacelle that are not modelled in the simulation. Therefore the blockage effect of these components does not exist in the simulation leading to the overestimation of the axial velocities. Unfortunately no measurements could be recorded for case 2.3. Although the spread amongst the partners is relatively big for this case the result from the TAU simulation compares fairly well with numerical results from other partners (see [4]) that also dispensed on the modelling of the spinner and nacelle. In comparison to simulations including the spinner and the nacelle again an overestimation of the streamwise velocity can be observed.

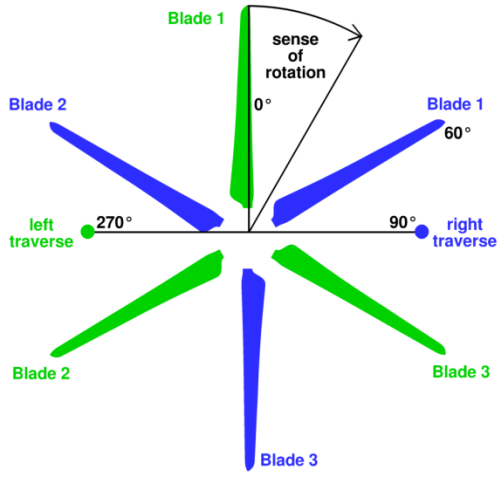

Figure 9: Rotor positions for measurements of the axial traverses: green rotor = 0° position, blue rotor = 60° position

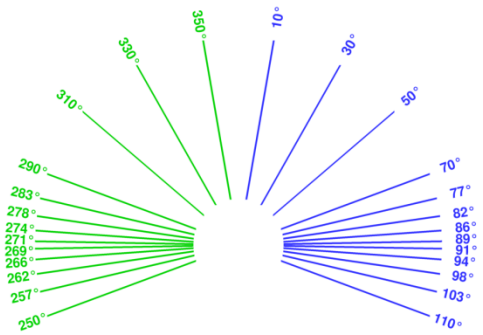

Figure 10: Rotor azimuth angles used for averaging the velocities for the radial traverses: green for positive y-traverse, blue for negative y-traverse

The axial velocities extracted from the radial traverses are not compared on an instantaneous basis. Moreover a weighted average is used in order to include the effect of large velocity variations around the blade passage. The azimuthal rotor positions used for computing the weighted average are depicted in **Figure 10**. While the azimuthal positions marked in green are used for the left side of the traverse (positive y-values in mcs), the azimuthal positions for the right side (negative y-values in mcs) are highlighted in blue.

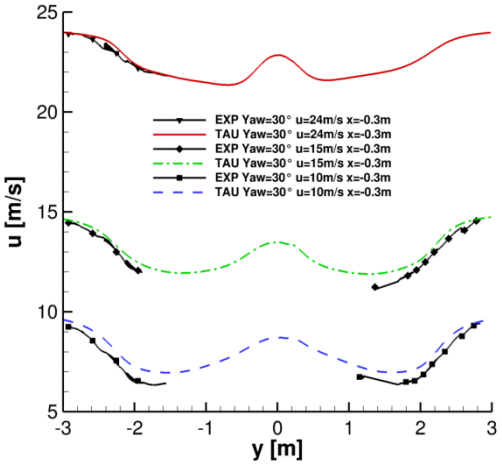

Figure 11: Streamwise velocity component (u) of the **upstream** radial traverse for all flow cases (case 2.3: solid red line; case 2.2: dotted dashed green line; case 2.1: dashed blue line)

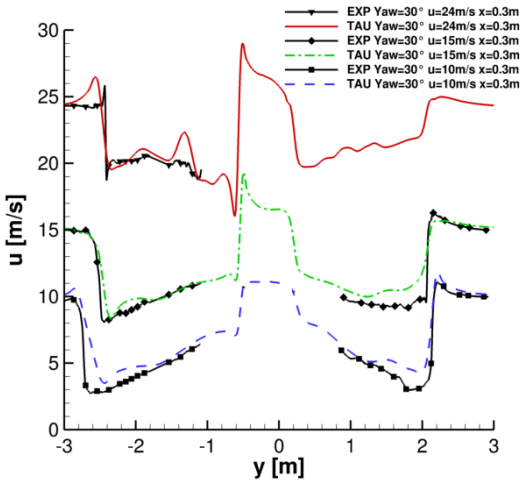

Figure 12: Streamwise velocity component (u) of the **downstream** radial traverse for all flow cases (case 2.3: solid red line; case 2.2: dotted dashed green line; case 2.1: dashed blue line)

The weighting coefficients used for determining the weighted average can be found in [4]. The velocities of the radial traverses are shown in **Figure 11** (upstream) and **Figure 12** (downstream). Note that positive y-values correspond to the left side of the rotor when looked at from upstream to downstream. The overall agreement is very good to excellent. The biggest differences occur for case 2.1 – both upstream and downstream. While for the upstream traverse the biggest difference is in the order of 0.5 m/s, the difference for the downstream traverse can reach up to 1 m/s on the left side of the traverse. For the other two cases the velocity differences are even smaller. In the case of the downstream traverses the agreement seems to be better for the right side of the rotor while on the left

side of the rotor bigger differences can be observed. The reason for this is not clear but might also be an effect of the omission of the spinner and nacelle. The latter can definitely be seen in the middle of the traverse for -1m < y < 1m. A better comparison can be achieved if the traverses are compared without averaging. (For this purpose six videos have been supplied as annex to this paper.)

5.2. Pressure distributions and local forces

During the comparison rounds also the normal and the tangential forces as well as pressure plots at five radial sections have been compared. Exemplarily four radial pressure plots and four graphs with normal/tangential forces are shown here. In the latter plots three different curves describing the experimental values are visible. This results from the fact that the trailing edge pressure (TEP) has not been measured during the experiment, but had to be reconstructed for computing integrated loads. The black curve (squares) named “Exp_Average” is obtained by averaging the values of the two pressure sensors (one on the upper and one on the lower surface of the profile) closest to the trailing edge. For the green curve (gradients) termed “Exp_Ave_of_Extr” the pressures of the last two pressure transducers on the upper side (and equivalent on the lower side) are extrapolated up to the trailing edge. The values from the upper and lower side are subsequently averaged. The blue curve (right triangles) is obtained by simply setting the TEP to zero. **Figure 13** depicts the normal force for case 2.3 at the 35% station as function of the azimuth angle. While the agreement between simulation and experiment is very good for the uprotating rotor blade (180° - 330° azimuth), differences become much more pronounced for the downrotating rotor blade (0° - 150°). Evidently besides the 1/rev fluctuation due to the yawing of the rotor a higher frequency phenomenon is present resulting in rapid changes of the normal force between 0° and 70° azimuth. The biggest differences occur around 90° azimuth angle. While the point of incipient separation (starting around 12 cm of the chord length) is predicted equally as can be seen in **Figure 15** quite severe differences arise on the first half of the suction side. At this part of the blade the turbulence model plays a much bigger role than in the other two flow cases, because the flow is massively separated. Apparently the simulation is not able to reproduce the unsteady flow phenomena in the root section in the same manner. Though it has to be kept in mind that the pressure distribution is averaged over many revolutions in case of the measurement whereas taken instantaneously in the case of the computation.

The normal force for case 2.2 at the 60% section is presented in **Figure 14**. As in the previous case the evaluation of the measurements using different TEP reconstructions show almost no differences. Since this is true for almost all sections of both flow cases (only for the 25% and 82% section of case 2.2 small differences are visible) it can be concluded that the TEP sensitivity for case 2.2 and case 2.3 is very small and can be neglected. On the other hand **Figure 14** demonstrates a substantial difference between the simulation and the experiment for the normal force at the 60% section. The reason for this is unclear. However, if the numerical results from other partners are included in the comparison as is done in [4] it seems likely that either the pressure measurement at this section is erroneous or some effect has been measured in the experiment that is not present in the simulation. This affects the normal and the tangential force in case 2.2 and case 2.1 (not shown here). Interestingly the results between the simulation and the experiment for the pressure distribution at this section agree very well as can be observed in **Figure 16**. The pressure plot can be viewed as representative for other azimuth angles because the agreement is similar for most of the azimuthal stations.

The tangential force for case 2.1 at the 82% section is presented in **Figure 17**. In contrast to the other flow cases a TEP sensitivity clearly exists for case 2.1. While the curves of the averaged TEP and the zero TEP almost coincide, a large offset to the curve of the extrapolated averaged TEP is evident. Furthermore the reader should note the small difference between the curve of the extrapolated averaged TEP and the simulation. The reason for the sensitivity on the TEP reconstruction becomes obvious in the pressure distribution depicted in **Figure 19**. Unfortunately various pressure transducers on the suction side were not working or had to be removed. Additionally a steep pressure gradient is present over the rear part of the airfoil section. This situation gives rise to larger errors in the experimental analysis which is shown by the huge sensitivity of the TEP reconstruction.

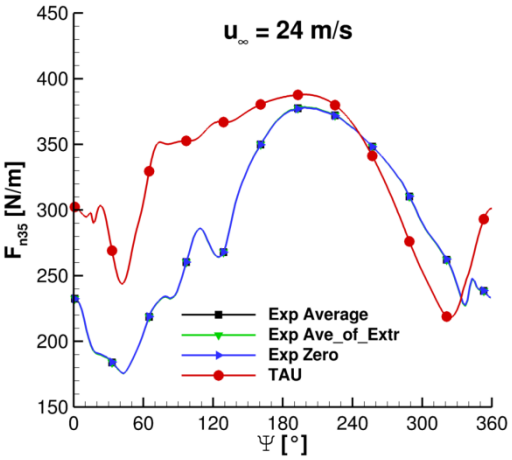

Figure 13: Normal force (F_n) for the **35%** section as a function of the azimuth angle for **case 2.3**: Experiment with TEP-average (black), Experiment with extrapolated TEP-average (green), Experiment with TEP = 0 (blue) and TAU (red), all experimental lines congruent

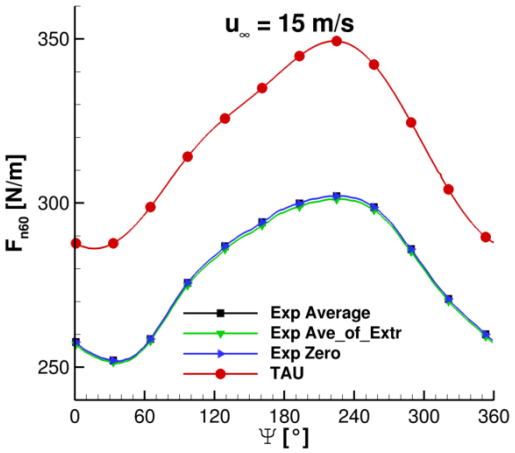

Figure 14: Normal force (F_n) for the **60%** section as a function of the azimuth angle for **case 2.2**: Experiment with TEP-average (black), Experiment with extrapolated TEP-average (green), Experiment with TEP = 0 (blue) and TAU (red)

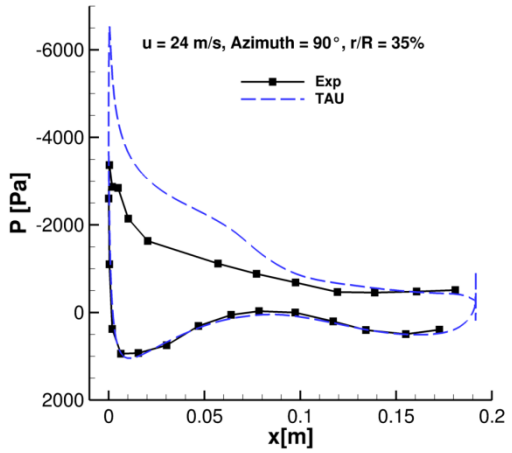

Figure 15: Pressure distribution of the **35%** section at 90° azimuth angle for **case 2.3**: Experiment (black, solid), TAU (blue, dashed)

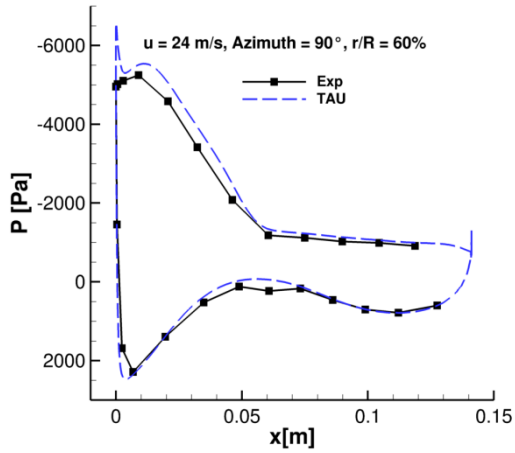

Figure 16: Pressure distribution of the **60%** section at 90° azimuth angle for **case 2.3**: Experiment (black, solid), TAU (blue, dashed)

Figure 18 shows the normal force for case 2.2 at the 92% section. As in the case of the 60% station the curves of the various experimental reconstruction techniques coincide. The simulated results also deviate substantially from the experiment. In contrast to the 60% section the normal force predicted by the simulation is smaller than measured in the experiment. The according pressure distribution is depicted in **Figure 20**. At first glance the pressure differences seem to be small as for the previous section. The reader should be reminded of the huge scale for the ordinate. Although seemingly small these differences add up to an average 30 N/m for the normal force for this section which is equivalent to 7.5%. The situation is even more severe for the tangential force at the 82% section. An average difference of 4 N/m (between "Exp_Average" and "TAU") is equivalent to 40%. (The pressure distributions for case 2.1 for a complete revolution have been supplied in five videos in the appendix.)

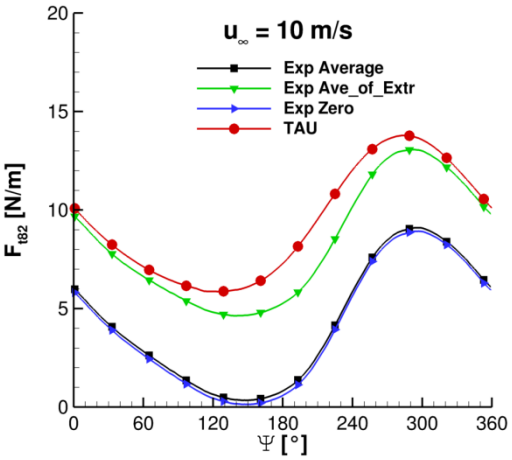

Figure 17: Tangential force (F_n) for the **82%** section as a function of the azimuth angle for **case 2.1**: Experiment with TEP-average (black), Experiment with extrapolated TEP-average (green), Experiment with TEP = 0 (blue) and TAU (red)

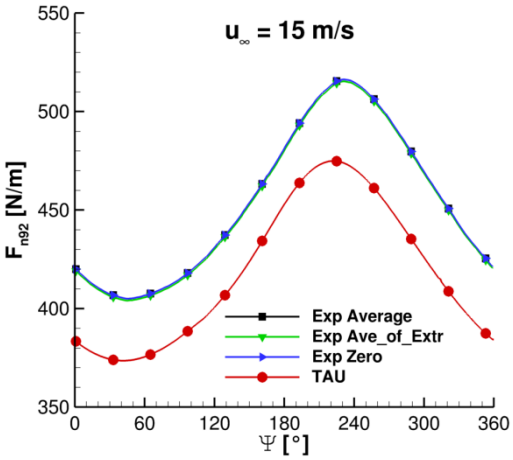

Figure 18: Normal force (F_n) for the **92%** section as a function of the azimuth angle for **case 2.2**: Experiment with TEP-average (black), Experiment with extrapolated TEP-average (green), Experiment with TEP = 0 (blue) and TAU (red), all experimental lines congruent

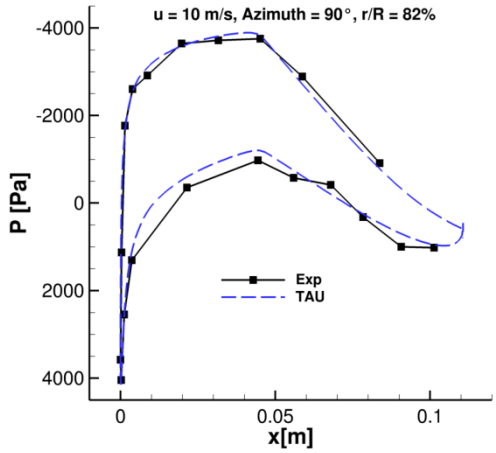

Figure 19: Pressure distribution of the **82%** section at 90° azimuth angle for **case 2.1**: Experiment (black, solid), TAU (blue, dashed)

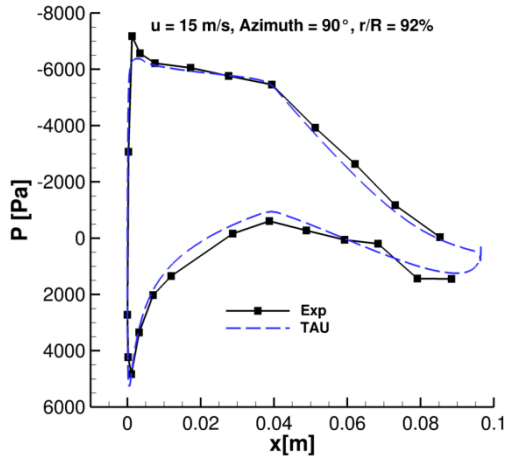

Figure 20: Pressure distribution of the **92%** section at 90° azimuth angle for **case 2.2**: Experiment (black, solid), TAU (blue, dashed)

5.3. Integral rotor loads

For the last comparison the local normal and tangential forces have to be integrated in order to obtain the rotor thrust and torque. For the experiment this is done applying the trapezoidal rule assuming zero loading at the blade root and tip. For the simulation three different approaches have been used: 1) all points of the CFD surface mesh ("TAU"), 2) only the radial sections used in the experiment, but all mesh points in chordwise direction ("TAU_r"), 3) CFD surface mesh coarsened in radial and chordwise direction such that for the integration only those points of the CFD mesh are used which are equivalent to the ones used in the experiment ("TAU_r+c"). The latter situation is shown exemplarily for one section in **Figure 22**. The rotor torque for case 2.2 for these different integration procedures is presented in **Figure 23**. As can be seen the difference between the experiment and the complete integration ("TAU") amounts to 15.1%. The radial coarsening reduces the difference to 11.6%. If the integration is performed exactly as in the experiment the difference is further diminished to a final 9.2%.

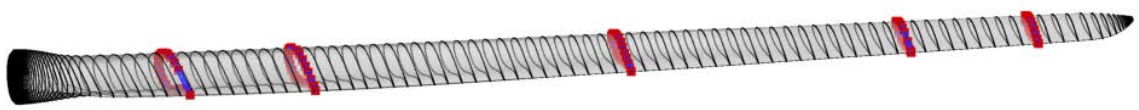

Figure 21: Radial discretization of the blade surface: TAU (black), Experiment (red, blue)

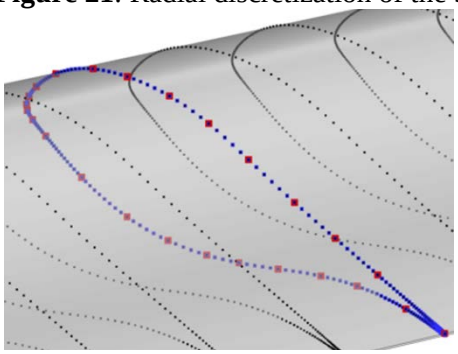

Figure 22: Chordwise discretization of CFD mesh (black) and location of pressure transducers (red)

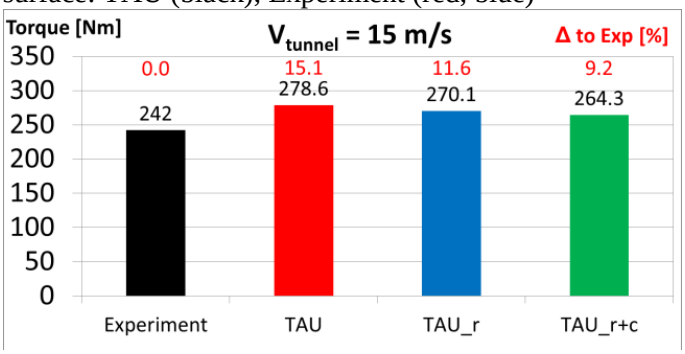

Figure 23: Rotor torque from various sources: Experiment (black), TAU all surface points (red), TAU radially reduced (blue), TAU exp. resolution (green)

Table 3: Results of integrated rotor thrust and torque for the experiment and the simulation

	Rotor thrust [N]				Rotor torque [Nm]			
	Exp	**TAU**	**TAU_r**	**TAU_r+c**	**Exp**	**TAU**	**TAU_r**	**TAU_r+c**
2.1	884	909	874	874	51	79.8	77.8	72.1
2.2	1480	1535	1475	1480	242	278.6	270.1	264.3
2.3	2012	2254	2211	2204	562	646.8	638	640.2

The results of the integrated rotor thrust and rotor torque of all flow cases are summarized in **Table 3**. The best agreement is achieved for the **rotor thrust** for case 2.1 and 2.2. Here the relative differences range between 0% and 1.2%. It should be mentioned that to some extend this might be also due to the lucky circumstance that local errors partly cancel out, e.g. the overprediction of the normal force at the 60% section (**Figure 14**) is compensated by the underprediction of the normal force at the 92% section (**Figure 18**). The biggest differences occur for the rotor torque for case 2.1. Although the difference between the experiment and the complete solution ("TAU") which amounts to 56.5% can be diminished to 41.4% by the radially and chordwise coarsening ("TAU_r+c"), the relative error can be considered huge. The difference could be further reduced to about 16%, if the method of the extrapolated averaged pressures was applied. Nevertheless the relative error in rotor torque for case 2.1 will probably always stay the highest due to the small absolute value. However, further improvements seem possible, if the measured values of the 60% section were analysed in more detail. The reason for this stems from the fact that the agreement amongst the numerical results of the various partners (see [4]) is very good, while the deviation of the experiment is much bigger than at any other section. The agreement between the experiment and the simulation for the rotor torque for case 2.2 can be regarded as fair after having been reduced to 9.2%. The differences of the rotor thrust and rotor torque for case 2.3 are located in the same range, namely 10% and 13% respectively. The differences seem to be attributed to the different separation prediction. Further improvements might be possible with a higher order turbulence model. On the other hand the flow is highly unsteady and therefore a relative difference of about 10% for this case does not seem bad.

6. Conclusion

Simulations of a model wind turbine under yawed conditions have been carried out with the DLR TAU code. The results have been converted in a special format in order to compare them with the experimental data that has been obtained in the DNW-LLF within the New Mexico campaign. Besides a simple comparison of the results as has also been done in the MexNext-III project, the data, especially of case 2.1, has been analysed in detail. Moreover it could systematically be shown that it is of utmost importance to assimilate the post-processing of the CFD results to the post-processing procedure of the experiment in order to obtain a good agreement for the integral values. Additionally the critical situation of the pressure sensor distribution on the suction side of the 82% section was highlighted and a method was proposed how to improve the results of the experiment at this section. Although the integral values compare fairly well after these adjustments, some errors seem to cancel out as can be seen by the comparison of the local normal and tangential forces. Overall a fair comparison between simulation and experiment has been reached.

Acknowledgements

The workshops were organized by the International Energy Agency (IEA-Wind) under Task 29. The author acknowledges the fruitful collaboration with all partners of the MexNext consortium and the experimental data provided by ECN. The author would specifically like to thank Koen Boorsma for fruitful discussions on the definitions and experimental data acquisition and data processing.

References

[1] H. Snel, J.G. Schepers, B. Montgomerie. The MEXICO project: the database and first results of data processing and interpretation. In *Proceedings of 47th AIAA Meeting*, Orlando, Florida, AIAA 2009-1217, 5-8 January 2009.

[2] K. Boorsma and J.G. Schepers. Rotor experiments in controlled conditions continued: New Mexico. *Journal of Physics: Conference Series, 753(2):022004, 2016.*

[3] K. Boorsma and J.G. Schepers. Description of Experimental Setup – New Mexico Experiment. *Technical Report ECN-X-15-093*, Jan 2018.

[4] J. G. Schepers and K. Boorsma et al. Final report of IEA Wind Task 29 Mexnext (Phase 3), *Technical report ECN-E--18-003*.

[5] D. Schwamborn, T. Gerhold and R. Heinrich. The DLR TAU-Code: Recent Applications in Research and Industry. In *Proceedings of European Conference on Computational Fluid Dynamics*, ECCOMAS CDF, Delft The Netherland, 2006.

[6] A. Bechmann, N.N. Sørensen and F. Zahle. CFD simulations of the MEXICO rotor, *Wind Energy Journal*, Vol 14, Issue 5, pages 677-689, 2011.

[7] P.-E. M. Réthoré, N. N. Sørensen, F. Zahle, A. Bechmann, and H. Aagaard Madsen. Mexico Wind Tunnel and Wind Turbine modelled in CFD. In AIAA Paper 2011-3373, 2011.

[8] T. Lutz, K. Meister and E. Krämer. Near Wake Studies of the MEXICO Rotor. *In Proceedings of EWEC 2011*, Brussels (BE), 14-17 Mar, 2011.

[9] N. N. Sørensen, A. Bechmann, P.-E. M. Réthoré, and F. Zahle. Near wake Reynolds-averaged Navier–Stokes predictions of the wake behind the MEXICO rotor in axial and yawed flow conditions. *Wind Energy*, 17(1):75–86, 2014.

[10] N. N. Sørensen, F. Zahle, K. Boorsma, J. G. Schepers. CFD computations of the second round of MEXICO rotor measurements. *Journal of Physics*: Conference Series **753** (2016) 022054.

[11] C. C. Heister, RANS Simulation of the New MEXICO Rotor Experiment Including Laminar-Turbulent Transition, *New Results in Numerical and Experimental Fluid Mechanics XI, Contributions to the 20th STAB/DGLR Symposium Braunschweig*, Germany, 2016, Vol. 136, 10.1007/978-3-319-64519-3, Springer International Publishing, 2018.

[12] F. R. Menter. Zonal two equation k-ω turbulence models for aerodynamic flows. AIAA Paper 1993-2906.